ADVANCED OPTICAL MATERIALS
www.advopticalmat.de

Ultralow-Loss Etchless Lithium Niobate Integrated Photonics at Near-Visible Wavelengths

*Yue Yu, Zejie Yu, Lai Wang, and Xiankai Sun**

Lithium niobate is considered as the "silicon of photonics" because of its many excellent optical properties as well as a wide transparency window covering the visible to mid-infrared wavelength range. Here, by using the principle of bound states in the continuum, lithium niobate integrated photonics at near-visible wavelengths with an etchless fabrication process is developed, which achieves a minimal propagation loss of 1.8 dB cm^{-1} in straight waveguides at the wavelength of ≈771 nm and a maximal intrinsic Q factor of 1.1×10^6 in disk microcavities at ≈765 nm. Typical integrated photonic components including Mach–Zehnder interferometers and multimode directional couplers are also demonstrated. Based on the experimental results, a convenient scheme of second-harmonic generation is proposed for converting light in the fundamental TE-polarized mode at a telecom wavelength into the second-order TM-polarized mode at a near-visible wavelength. The demonstrated etchless lithium niobate integrated photonic platform can support both passive and active optical devices and systems on a chip for various visible-light applications including optical imaging, nonlinear optics, and quantum information processing.

1. Introduction

Photonic integration provides a path to reduce device size, weight, power consumption, and improve manufacturability at the chip scale. Photonic integrated circuits have developed drastically in the past decades and have enabled many applications in a wide optical wavelength range. Compared with the integrated platforms and devices at the telecom wavelengths, visible integrated photonics has been less developed. Targeting at its distinctive applications in biosensing[1–3] and optogenetics,[4,5] quantum information processing,[6–9] and frequency metrology,[10,11] people have investigated visible integrated photonics in various materials including SiO_2,[12,13] Si_3N_4,[14–20] InP,[21,22] diamond,[23–27] TiO_2,[28] AlN,[29] and lithium niobate.[30] Among these materials, lithium niobate is regarded as the most promising candidate because of its ultrabroad optical transparency window (350–5200 nm), large electro-optic coefficients, and large second-order optical nonlinearity.[31] These advantages have enabled many nonlinear applications in frequency metrology and quantum information processing in a wide wavelength range.

A thin-film lithium-niobate-on-insulator (LNOI) technology has significantly extended the application areas because of the strong optical confinement and high photonic integration density.[32] Pivotal photonic devices with excellent performance have been demonstrated on lithium niobate platforms, such as high-speed modulators,[33–36] single-photon sources,[37–39] and supercontinuum light emitters.[40] However, photonic integrated circuits fabricated on the LNOI platform usually require high-quality etching of lithium niobate, which adds to device fabrication difficulty and reduces device yield. The device performance also depends critically on the quality of etching. Recently, a fundamentally new photonic architecture by patterning a fabrication-friendly optically transparent material on an optically functional substrate was theoretically proposed[41] and experimentally demonstrated without the need for etching of the substrate.[42] This photonic architecture can guide and route photons with ultralow optical loss by engineering its geometric parameters to eliminate the dissipation to the substrate continuum. Consequently, this photonic architecture has enabled an etchless lithium niobate integrated platform, with experimental demonstrations of high-dimensional communication, acousto-optic modulation, and 2D-material integration at the telecom wavelengths.[43–45] Based on this principle, here we developed an ultralow-loss etchless lithium niobate integrated photonic platform at near-visible wavelengths (765–781 nm) and experimentally realized the core photonic components including waveguides, microcavities, Mach–Zehnder interferometers, and multimode directional couplers. With excellent performance and simple fabrication processes, the demonstrated photonic integrated circuits and the photonic components will enable on-chip applications of optical imaging, optogenetics, and quantum information processing in the near-visible wavelength range.

Y. Yu, Dr. Z. Yu,[+] Prof. X. Sun
Department of Electronic Engineering
The Chinese University of Hong Kong
Shatin, New Territories, Hong Kong
E-mail: xksun@cuhk.edu.hk

Prof. L. Wang
Beijing National Research Center for Information Science and Technology (BNRist)
Department of Electronic Engineering
Tsinghua University
Beijing 100084, China

The ORCID identification number(s) for the author(s) of this article can be found under https://doi.org/10.1002/adom.202100060.

[+]Present address: College of Optical Science and Engineering, Zhejiang University, Hangzhou, Zhejiang 310058, China

DOI: 10.1002/adom.202100060

2. Results and Discussion

Figure 1a illustrates the photonic integrated circuit fabricated on a LNOI substrate with an etchless process. Figure 1b shows the cross section of the waveguide structure, which is constructed by patterning a fabrication-friendly optically transparent polymer (ZEP520A) on a *z*-cut LNOI substrate. The thicknesses of the lithium niobate layer, the polymer atop, and the silicon oxide underneath are 150 nm, 400 nm, and 2 µm, respectively. Similar to the bound states in the continuum (BICs) demonstrated for the telecom band at ≈1550 nm, we could engineer the geometry of the polymer waveguide to obtain BICs in the near-visible band at ≈775 nm. We adopted a finite-element method in COMSOL to analyze the modes supported by the waveguide structure in Figure 1b, where the refractive indices of lithium niobate were set as $n_o = 2.2592$, $n_e = 2.1789$, and the refractive index of the polymer was set as 1.5492 at the wavelength of 771 nm. Figure 1c plots the effective refractive index distributions for both the TE and TM polarizations. The patterned polymer waveguide extending in the *y* direction renders a high-effective-index channel for both TE- and TM-polarized light. Figure 1d shows cross-sectional |**E**| profiles of a TE continuous mode and the fundamental TM bound mode. Because the TM-polarized bound mode lies in the TE-polarized continuum, the former can interact with the latter, leading to energy dissipation into the substrate continuum. Nonetheless, by carefully engineering the waveguide structural parameters, the interaction between the TM bound mode and the TE continuous modes can be eliminated, where the TM bound mode turns into the desired BIC.

To develop lithium niobate photonic integrated circuits based on BICs in the near-visible wavelength range, one needs to obtain the elementary photonic components such as waveguides and microcavities. **Figure 2**a,b illustrates straight and bent waveguides on the etchless lithium niobate integrated platform, respectively. The propagation loss of these waveguides is caused mainly by the energy dissipation at the two waveguide edges into the continuous modes, and the total loss is a coherent addition of energy dissipation through the two dissipation channels. Therefore, the propagation loss is a result of interference between the two dissipation channels and depends on the waveguide geometric parameters. Figure 2c,d shows the propagation loss of the TM bound mode at the wavelength of 771 nm in a straight and a bent waveguide, respectively. It is clear that the propagation loss can be eliminated for certain geometric parameters when perfect destructive interference is achieved, corresponding to the attainment of BIC. For waveguides with those geometric parameters, the TM bound mode is entirely decoupled from the TE continuous modes, becoming the desired BIC. However, it should be noted that although the loss to the substrate continuum can be eliminated by using the principle of BIC, the conventional bending loss to the free space cannot be avoided.[42] This is reflected in the fact that the quality factor of a microdisk cavity drops drastically when its

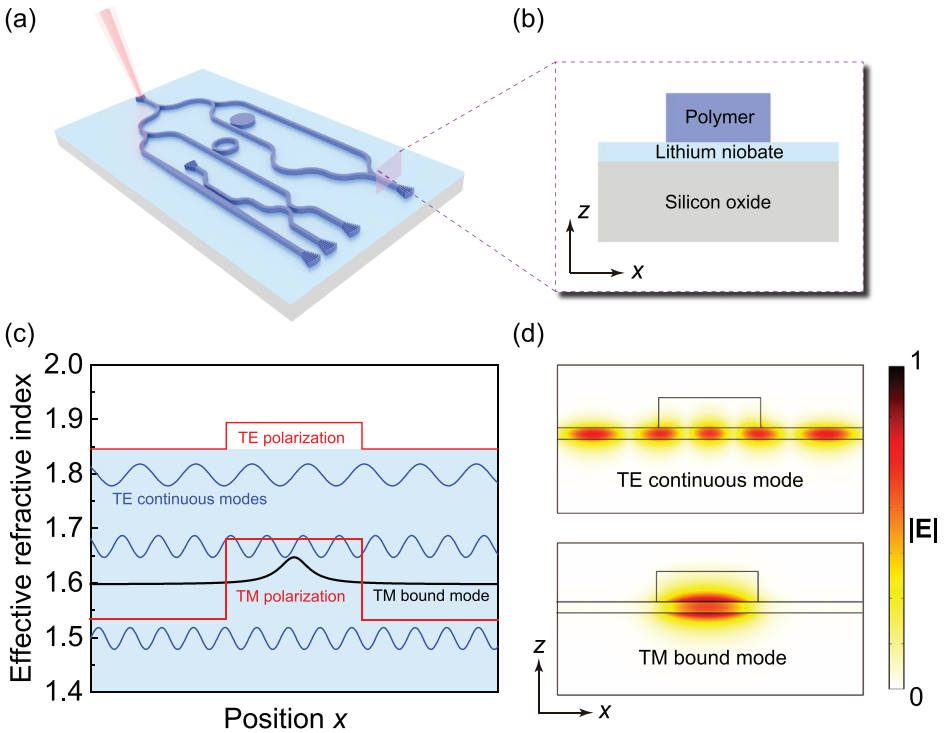

Figure 1. a) Schematic illustration of the photonic integrated circuit fabricated on a LNOI substrate with an etchless process. b) Cross section of the waveguide structure supporting the photonic BIC. The bottom is a thick layer of silicon oxide (gray), the middle is a thin layer of lithium niobate (light blue), and the top is a thin patterned polymer waveguide (dark blue). c) Effective refractive index distributions of the waveguide structure in (b) for the TE and TM polarizations. d) Electric field |**E**| profiles of the TE continuous mode (top) and the TM bound mode (bottom) supported by the waveguide structure in (b).

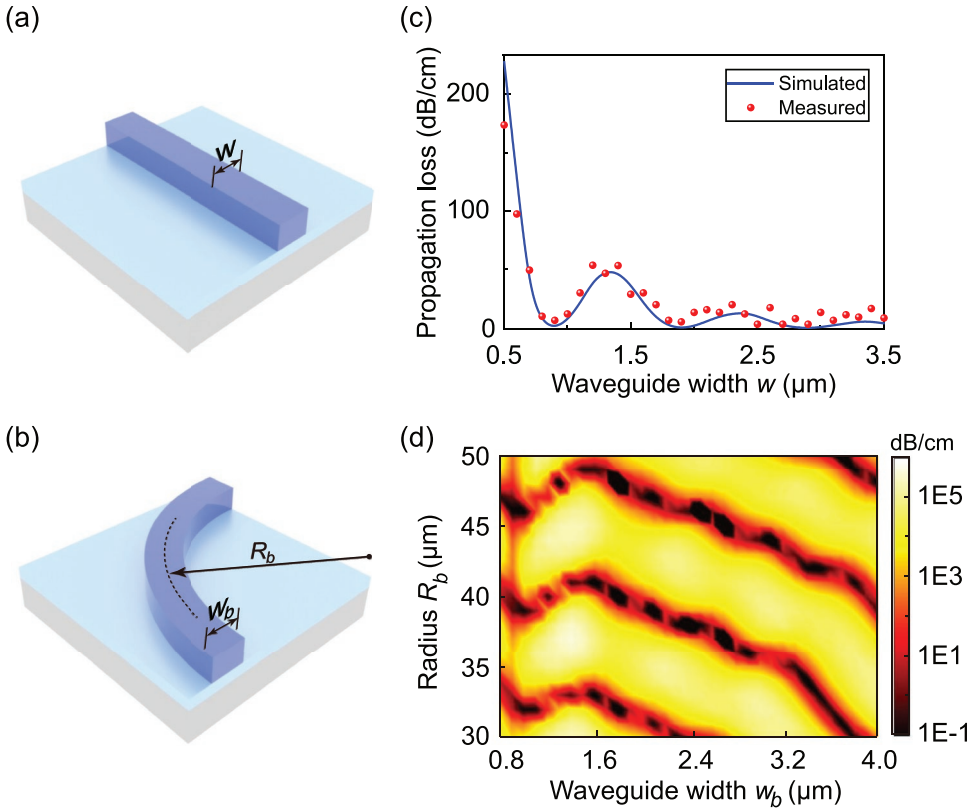

Figure 2. a) Illustration of a straight waveguide with the waveguide width being w. b) Illustration of a bent waveguide with the bend radius and waveguide width being R_b and w_b, respectively. c) Propagation loss of the straight waveguide in (a) as a function of the waveguide width w at the wavelength of 771 nm. The blue line plots the simulated result, and the red dots represent the measured data. d) Simulated propagation loss of the bent waveguide in (b) as a function of the bend radius R_b and waveguide width w_b at the wavelength of 771 nm.

radius is less than 30 μm but can be regarded as infinity when its radius is sufficiently large (see Figure S2c, Supporting Information). In practice, the optical loss is ultimately limited by the material absorption and fabrication imperfection, rather than the radiation into the substrate.

We fabricated straight waveguides with different waveguide widths on a LNOI substrate and measured their propagation loss. We adopted grating couplers, which were fabricated along with the waveguides with the same etchless process, for coupling light between optical fibers and the on-chip waveguides. These grating couplers are polarization sensitive and were designed for optimal coupling of the TM-polarized light. With a period of 0.62 μm and a duty cycle of 0.42, they achieved a coupling efficiency of 12.7% per coupler at the center wavelength of 771.8 nm and a 3-dB bandwidth of 10 nm, with the light incident angle of 22°. Light from a tunable semiconductor laser was sent through a fiber polarization controller before being coupled into a fabricated device via the input grating coupler. The light transmitted through the waveguide was coupled out of chip via the output grating coupler and then collected by a power meter. To measure the propagation loss of a straight waveguide with a certain width, we fabricated on the same chip two straight waveguides with the same width but different lengths. By comparing the transmissions of these two devices, we could extract the propagation loss of waveguide at this width. Figure 2c shows that the measured propagation loss of straight waveguides with different waveguide widths agrees well with the simulated result. A propagation loss of 1.8 dB cm^{-1} is obtained at the waveguide width of 2.5 μm. Figure 2d shows the simulated propagation loss of bent waveguides as a function of the bend radius and waveguide width. Based on the simulated and measured results in Figure 2c,d, we chose the width of both straight and bent waveguides as 1.8 μm and the bend radius as 40 μm to obtain low propagation loss and compact device size.

We also fabricated microdisk and microring cavities to demonstrate 3D confinement of photons based on BICs. **Figure 3**a shows an optical microscope image of a fabricated microdisk cavity, along with an evanescently coupled bus waveguide and grating couplers. Figure 3b is a top-view image of the device when a light field is coupled into the device and resonating inside the microdisk cavity. The nonuniformly distributed light field is probably due to extra scattering by particles on the edge of the microdisk cavity. The Q factors could be measured from the transmission spectra of the waveguide evanescently coupled with the cavity. Figure 3c plots the simulated and experimental intrinsic Q factor of the microdisk cavity as a function of the disk radius R_d. The experimental intrinsic Q factors were calculated from the measured loaded Q factors and extinction ratios based on the under-coupling condition (Section 1, Supporting Information). The experimental result agrees well with the simulated result, both of which confirm the attainment of BIC when the disk radius R_d is 79.3 μm. Figure 3d plots

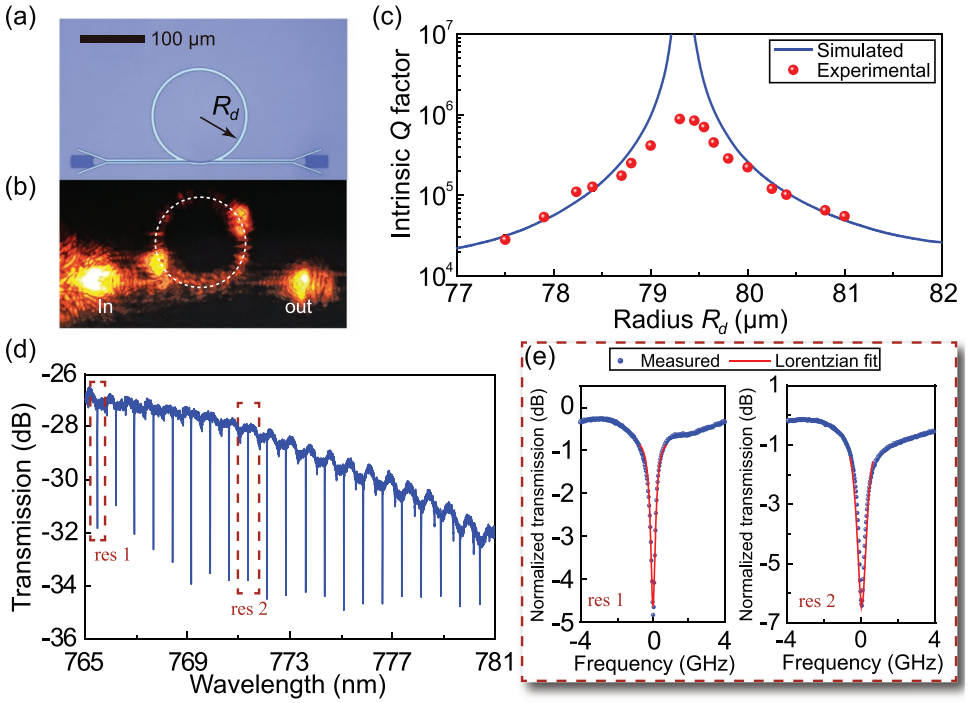

Figure 3. a) Optical microscope image of a fabricated device including a microdisk cavity, a coupling waveguide, and two grating couplers. b) Top-view image of the device in (a) when a light field is coupled into the device and resonating inside the microdisk cavity. The white dashed circle marks the periphery of the microdisk cavity. c) Simulated and experimental intrinsic Q factor of the microdisk cavity as a function of the disk radius R_d. d) Measured optical transmission spectrum of a microdisk cavity whose geometric parameters satisfy the BIC condition for light at the wavelength of ≈771 nm. e) Zoomed-in spectra of two cavity resonances marked in (d), showing the loaded (intrinsic) Q factors of 8.8×10^5 (1.1×10^6) and 6.1×10^5 (8.8×10^5) at the wavelengths of 765.4 and 771.3 nm, respectively.

the measured transmission spectrum of a microdisk cavity with R_d = 79.3 μm. Figure 3e plots the zoomed-in spectra of the two cavity resonances marked in Figure 3d, showing the loaded (intrinsic) Q factors of 8.8×10^5 (1.1×10^6) and 6.1×10^5 (8.8×10^5) at the wavelengths of 765.4 and 771.3 nm, respectively. The achieved intrinsic Q factor is twice higher than that of a device fabricated by etching lithium niobate, where an intrinsic Q factor of 5.3×10^5 was obtained at 733 nm.[30] Compared with our previous work in the telecom band, the Q factors for the BICs at the near-visible wavelengths are about four times higher, which can be attributed to lower optical absorption of the polymer ZEP520A in this wavelength range. The experimental results of microring cavities are presented in Section 2 of the Supporting Information.

Based on the developed BIC waveguides, we also constructed and demonstrated some elementary photonic components for photonic integrated circuits on this integrated platform. **Figure 4**a,b shows our fabricated Mach–Zehnder interferometer and directional coupler, respectively. Figure 4c shows the measured optical transmission spectrum for the Mach–Zehnder interferometer. Light coupled into the input port is divided by a power splitter into the two arms of the Mach–Zehnder interferometer. The lengths of the two arms are unequal, and thus the interference of light in the two arms produces wavelength-dependent transmission at the output as shown in Figure 4c. The relatively low extinction ratio is attributed to the unequal propagation loss experienced by light after traveling through the two arms of unequal lengths. Figure 4d shows the measured optical transmission spectra for the directional coupler with an optimal coupling length, which indicates that light can be directed efficiently from one waveguide channel to another in the wavelength range of 765–781 nm.

Next, we investigated multimode directional couplers on this integrated platform. They can convert a BIC of the fundamental order into a BIC of a higher order and thus are the building block for high-dimensional optical communication systems. By carefully optimizing the widths of different waveguides and the coupling lengths between them, multiple light signals from multiple channels can propagate in a single waveguide without interfering with each other, which can significantly enhance data link capacity to meet the increasing demand for high data rates in on-chip optical communication. The waveguide widths for BICs of different orders were chosen to satisfy two requirements: low propagation loss and phase matching between the BICs of different orders. The design details are presented in Section 3 of the Supporting Information. **Figure 5**a shows an optical microscope image of a fabricated TM_0–TM_1 directional coupler with a close-up view of its coupling region. The waveguides that support BICs of different orders are labeled as wg_0 and wg_1, with their widths being w_0 and w_1, respectively. The gap between waveguides wg_0 and wg_1 is g_1. The coupling length for converting the TM_0 mode into the TM_1 mode is L_1. Setting the same effective refractive index of 1.682 for all the BICs of different orders, we obtained these optimized parameters: w_0 = 1.86 μm,

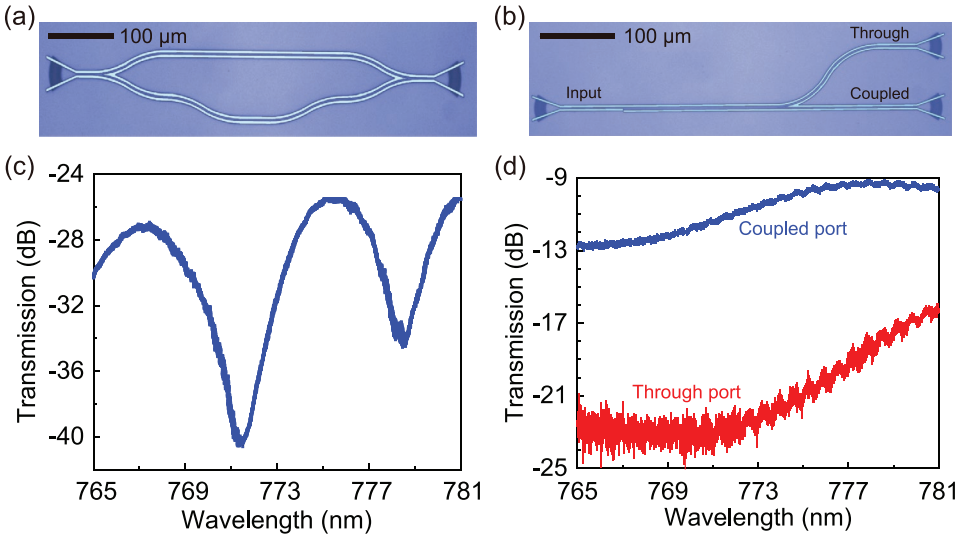

Figure 4. a,b) Optical microscope images of a fabricated Mach–Zehnder interferometer (a) and directional coupler (b). c,d) Measured optical transmission spectra for the Mach–Zehnder interferometer (c) and directional coupler (d).

w_1 = 4.04 μm, g_1 = 180 nm, and L_1 = 276 μm. The details for the TM_0–TM_2 directional coupler are presented in Section 4 of the Supporting Information. Figure 5b shows the simulated normalized transmission of the coupled and through ports at the wavelength of 771 nm for the TM_0–TM_1 directional coupler as a function of the coupling length. Figure 5c shows the simulated normalized transmission spectra of the coupled and through ports of the TM_0–TM_1 directional coupler with the theoretical optimal coupling length of 276 μm. Figure 5d shows the simulated electric field profile (|**E**|) of light coupled from the TM_0 mode in the upper waveguide to the TM_1 mode in the lower waveguide in the mode conversion region of the TM_0–TM_1 directional coupler, which confirms successful mode conversion with the optimal coupling length of 276 μm. Figure 5e,f shows the experimental results of the fabricated TM_0–TM_1 directional couplers. In Figure 5e, the solid lines are fits of the experimental data by using a sinusoidal function, which reveal that the experimental optimal coupling length is L_1 = 325 μm. Figure 5f plots the measured normalized transmission spectra of the coupled and through ports of the TM_0–TM_1 directional coupler with the experimental optimal coupling length of 325 μm. The difference between the experimental and simulated results can be attributed to the unavoidable structural deviations in device fabrication. These experimental results have demonstrated successful mode conversion in the multimode directional couplers, which can be used for constructing (de)multiplexers for high-dimensional communication on the lithium niobate integrated platform.

In addition to the above demonstrated devices, this etchless platform has great potential in developing various applications by exploiting the unique properties of lithium niobate. With its large electro-optic coefficients, we can integrate the hybrid waveguides with electrodes to build electro-optic modulators, optical switches, and routers, where the refractive indices are controlled by an electric field between the electrodes. With its large photoelastic coefficients, we can realize efficient acousto-optic modulation by integrating the hybrid waveguides with interdigital transducers to build acousto-optic modulators, optical isolators, and circulators. Furthermore, lithium niobate is also well known for its large second-order nonlinear optical coefficients, which can be used for nonlinear frequency conversion and entangled photon-pair generation. Here, we theoretically propose a scheme of second-harmonic generation of light on this platform and numerically analyze the conversion efficiency. In a quadratic nonlinear waveguide, the normalized conversion efficiency is expressed as[46,47]

$$\eta = \frac{8\pi^2}{\varepsilon_0 c n_1^2 n_2 \lambda^2} \frac{\zeta^2 d_{\text{eff}}^2}{A_{\text{eff}}} \text{sinc}^2\left(L\Delta k/2\right) \quad (1)$$

where d_{eff} is the effective nonlinear coefficient, λ is the fundamental wavelength, n_1 and n_2 are the effective refractive indices of the fundamental and second-harmonic modes, respectively, A_{eff} is the effective modal area, ζ is the spatial modal overlap factor between the fundamental and second-harmonic modes, L is the waveguide length, and Δk is the mismatch of wave numbers. First, let us examine the possibility of phase matching between the $TE_{0,\text{tele}}$ mode at the telecom wavelengths and the $TM_{0,\text{vis}}$, $TM_{1,\text{vis}}$, $TM_{2,\text{vis}}$ modes at the near-visible wavelengths in a straight waveguide. With a finite-element method, we simulated the effective refractive indices (**Figure 6**a) of the four modes, with their modal field profiles shown in Figure 6b, as a function of the waveguide width and wavelength (at telecom wavelengths for the $TE_{0,\text{tele}}$ mode and at near-visible wavelengths for the $TM_{0,\text{vis}}$, $TM_{1,\text{vis}}$, and $TM_{2,\text{vis}}$ modes). The intersecting line of the surfaces for the $TE_{0,\text{tele}}$ and $TM_{2,\text{vis}}$ modes corresponds to phase matching of these two modes. Figure 6c shows that phase matching between the $TE_{0,\text{tele}}$ mode at the fundamental wavelength of 1550 nm and the $TM_{2,\text{vis}}$ mode at the second-harmonic wavelength of 775 nm can be achieved in straight waveguides with a waveguide width of 2.30 μm, as indicated by the arrow. Figure 6d plots the phase-matched fundamental wavelength and the propagation loss of the $TM_{2,\text{vis}}$

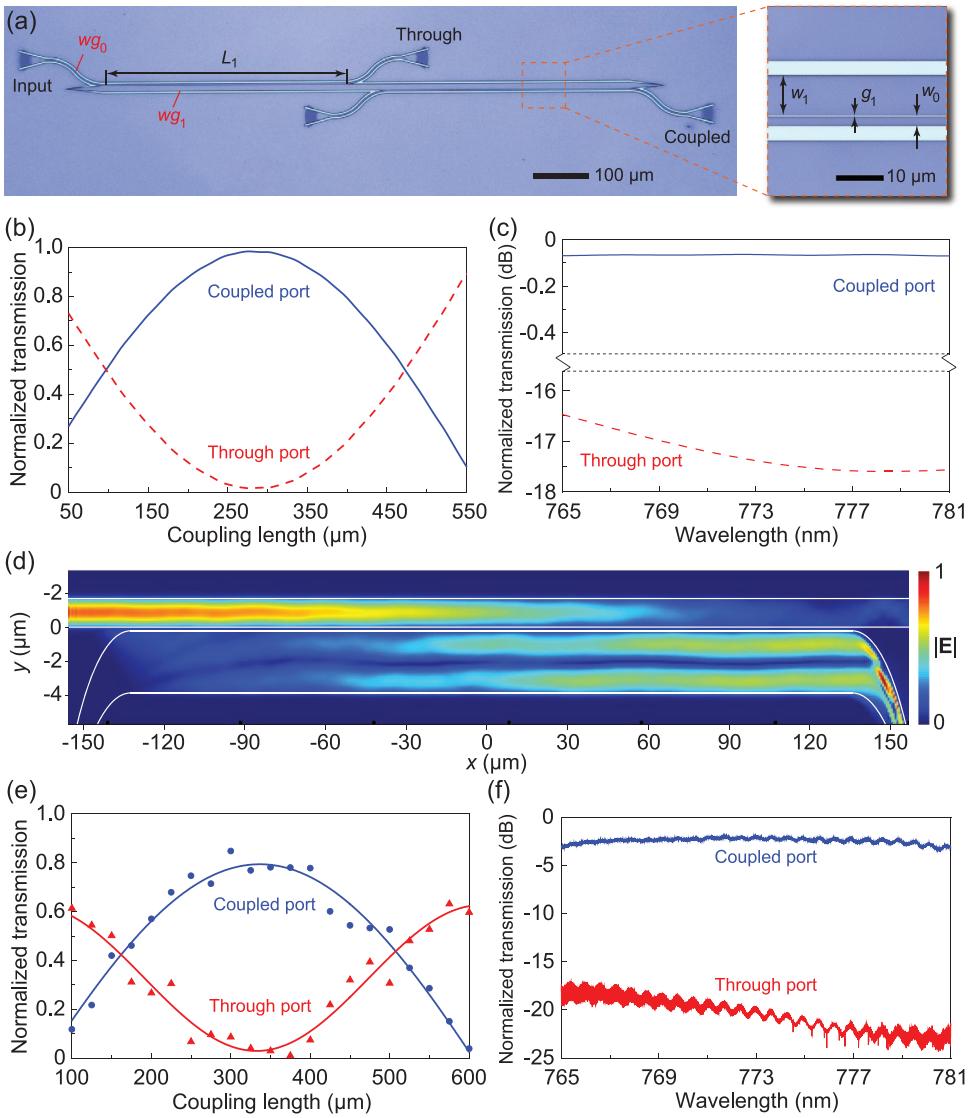

Figure 5. a) Optical microscope image (left) of a fabricated TM_0–TM_1 directional coupler and a close-up view (right) of its coupling region. b) Simulated normalized optical transmission of the coupled (blue solid line) and through (red dashed line) ports at the wavelength of 771 nm for the TM_0–TM_1 directional coupler as a function of the coupling length. c) Simulated normalized optical transmission spectra of the coupled (blue solid line) and through (red dashed line) ports of the TM_0–TM_1 directional coupler with the theoretical optimal coupling length of 276 μm. d) Simulated electric field |**E**| profile of light coupled from the TM_0 mode in the upper waveguide to the TM_1 mode in the lower waveguide in the mode conversion region of the TM_0–TM_1 directional coupler with the coupling length of 276 μm. e) Measured normalized optical transmission of the coupled (blue dots) and through (red triangles) ports at the wavelength of 771 nm for the TM_0–TM_1 directional coupler as a function of the coupling length. The solid lines are fits of the experimental data by using a sinusoidal function. f) Measured normalized optical transmission spectra of the coupled (blue line) and through (red line) ports of the TM_0–TM_1 directional coupler with the experimental optimal coupling length of 325 μm.

mode as a function of the waveguide width. It is found that the phase-matched fundamental wavelength follows a linear relationship with the waveguide width. When the waveguide width is 2.65 μm, a theoretical zero propagation loss is obtained for the $TM_{2,vis}$ mode (corresponding to the attainment of BIC) while the phase-matched fundamental (second-harmonic) wavelength is 1646.6 nm (823.3 nm). Because the $TE_{0,tele}$ mode is a regular bound state, its propagation loss is theoretically zero if the structure roughness and material absorption can be neglected. With the waveguide design parameters and the assumed nonlinear coefficient $d_{31} = -4.3$ pm V^{-1},[48] we numerically obtained $A_{eff} = 20.3\ \mu m^2$, $\zeta = 0.14$, and $\eta = 0.48\%\ W^{-1}\ cm^{-2}$. For further improvement of the conversion efficiency, we can resort to periodic poling of lithium niobate to achieve quasi-phase matching between other waveguide modes (e.g., $TE_{0,tele}$ and $TM_{0,vis}$, $TM_{0,tele}$ and $TM_{0,vis}$).

3. Conclusion

In summary, with an etchless fabrication process, we developed an ultralow-loss lithium niobate integrated photonic platform

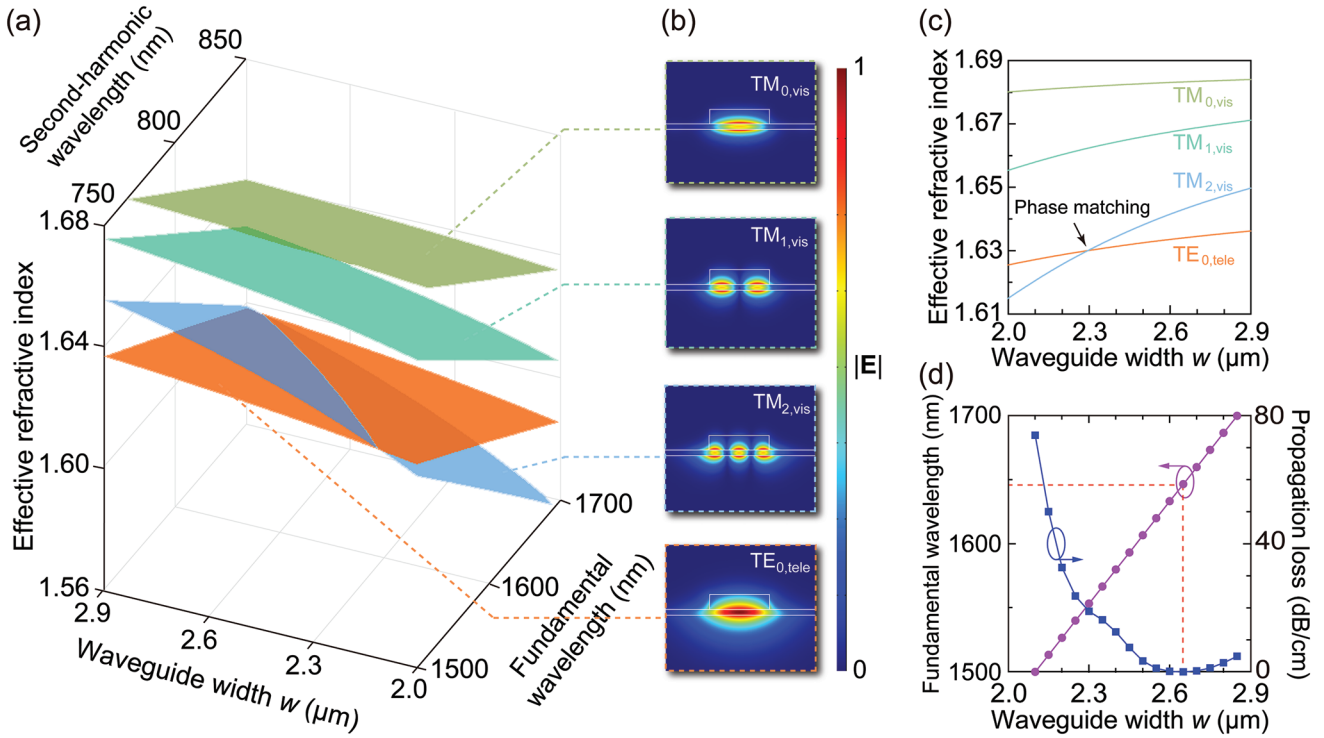

Figure 6. a) Simulated effective refractive indices of the $TE_{0,tele}$, $TM_{0,vis}$, $TM_{1,vis}$, and $TM_{2,vis}$ modes in a straight waveguide as a function of the waveguide width and wavelength (at telecom wavelengths for the $TE_{0,tele}$ mode and at near-visible wavelengths for the $TM_{0,vis}$, $TM_{1,vis}$, and $TM_{2,vis}$ modes). b) Simulated |**E**| modal field profiles of the four modes. c) Simulated effective refractive index as a function of the waveguide width w at the wavelength of 1550 nm for the $TE_{0,tele}$ mode and 775 nm for the $TM_{0,vis}$, $TM_{1,vis}$, and $TM_{2,vis}$ modes. The arrow indicates the point of phase matching between the $TE_{0,tele}$ mode at the fundamental wavelength and the $TM_{2,vis}$ mode at the second-harmonic wavelength. d) The phase-matched fundamental wavelength and propagation loss of the $TM_{2,vis}$ mode as a function of the waveguide width w.

and experimentally demonstrated multiple integrated photonic components at near-visible wavelengths (765–781 nm). We also proposed a convenient scheme to achieve second-harmonic generation on this platform for converting light at a telecom wavelength to a near-visible wavelength. Based on the principle of BICs, we experimentally achieved a minimal propagation loss of 1.8 dB cm^{-1} in straight waveguides at the wavelength of ≈771 nm and a maximal intrinsic Q factor of 1.1×10^6 in disk microcavities at ≈765 nm. The optical loss can be further reduced by optimizing the fabrication processes. For example, the optical absorption loss can be reduced by replacing the polymer with another optically transparent material such as silicon oxide. The scattering loss caused by sidewall roughness can be reduced by performing a baking step after lithographic patterning of the polymer. The demonstrated etchless integrated photonic platform is versatile for different wavelength ranges, different substrates, and integration with different functional materials. For example, when integrated with optically active materials such as perovskites, 2D transition metal dichalcogenides, and polymers doped with dye molecules, this platform facilitates exploration of on-chip high-speed photodetectors, optical amplifiers, and low-threshold lasers at near-visible wavelengths. With strong electro-optic, piezoelectric, and optical nonlinear effects of lithium niobate, this ultralow-loss etchless integrated photonic platform paves the way for both passive and active devices and applications in the visible regime, such as optical imaging, optogenetics, and quantum information processing.

Supporting Information

Supporting Information is available from the Wiley Online Library or from the author.

Acknowledgements

This work was supported by the Research Grants Council of Hong Kong (14208717, 14206318, 14209519, N_CUHK415/15) and the National Natural Science Foundation of China (51561165012).

Conflict of Interest

The authors declare no conflict of interest.

Data Availability Statement

The data that support the findings of this study are available from the corresponding author upon reasonable request.

Keywords

bound states in the continuum, etchless process, integrated photonics, lithium niobate, visible photonics

Received: January 10, 2021
Revised: April 25, 2021
Published online: August 19, 2021

[1] P. Muellner, E. Melnik, G. Koppitsch, J. Kraft, F. Schrank, R. Hainberger, *Procedia Eng.* **2015**, *120*, 578.
[2] T. Claes, W. Bogaerts, P. Bienstman, *Opt. Express* **2010**, *18*, 22747.
[3] I. Goykhman, B. Desiatov, U. Levy, *Appl. Phys. Lett.* **2010**, *97*, 081108.
[4] E. Shim, Y. Chen, S. Masmanidis, M. Li, *Sci. Rep.* **2016**, *6*, 22693.
[5] E. Segev, J. Reimer, L. Moreaux, T. Fowler, D. Chi, W. Sacher, M. Lo, K. Deisseroth, A. Tolias, A. Faraon, M. Roukes, *Neurophotonics* **2016**, *4*, 1.
[6] A. I. Lvovsky, B. C. Sanders, W. Tittel, *Nat. Photonics* **2009**, *3*, 706.
[7] K. F. Reim, P. Michelberger, K. C. Lee, J. Nunn, N. K. Langford, I. A. Walmsley, *Phys. Rev. Lett.* **2011**, *107*, 053603.
[8] O. Katz, O. Firstenberg, *Nat. Commun.* **2018**, *9*, 2074.
[9] D. F. Phillips, A. Fleischhauer, A. Mair, R. L. Walsworth, M. D. Lukin, *Phys. Rev. Lett.* **2001**, *86*, 783.
[10] T. Udem, R. Holzwarth, T. W. Hänsch, *Nature* **2002**, *416*, 233.
[11] J. Kitching, E. A. Donley, S. Knappe, M. Hummon, A. T. Dellis, J. Sherman, K. Srinivasan, V. A. Aksyuk, Q. Li, D. Westly, B. Roxworthy, A. Lal, *J. Phys.: Conf. Ser.* **2016**, *723*, 012056.
[12] Y. Gong, J. Vučković, *Appl. Phys. Lett.* **2010**, *96*, 031107.
[13] S. H. Lee, D. Y. Oh, Q.-F. Yang, B. Shen, H. Wang, K. Y. Yang, Y.-H. Lai, X. Yi, X. Li, K. Vahala, *Nat. Commun.* **2017**, *8*, 1295.
[14] P. Muñoz, G. Micó, L. A. Bru, D. Pastor, D. Pérez, J. Doménech, J. Fernández, R. Baños Lopez, B. Gargallo, R. Alemany, A. Sánchez, J. Cirera, R. Mas, C. Domínguez, *Sensors* **2017**, *17*, 2088.
[15] S. Romero-García, F. Merget, F. Zhong, H. Finkelstein, J. Witzens, *Opt. Express* **2013**, *21*, 14036.
[16] E. S. Hosseini, S. Yegnanarayanan, A. H. Atabaki, M. Soltani, A. Adibi, *Opt. Express* **2009**, *17*, 14543.
[17] M. Khan, T. Babinec, M. W. McCutcheon, P. Deotare, M. Lončar, *Opt. Lett.* **2011**, *36*, 421.
[18] C. G. H. Roeloffzen, L. Zhuang, C. Taddei, A. Leinse, R. G. Heideman, P. W. L. van Dijk, R. M. Oldenbeuving, D. A. I. Marpaung, M. Burla, K. J. Boller, *Opt. Express* **2013**, *21*, 22937.
[19] D. J. Moss, R. Morandotti, A. L. Gaeta, M. Lipson, *Nat. Photonics* **2013**, *7*, 597.
[20] W. D. Sacher, Y. Huang, G.-Q. Lo, J. K. S. Poon, *J. Lightwave Technol.* **2015**, *33*, 901.
[21] R. Nagarajan, M. Kato, D. Lambert, P. Evans, S. Corzine, V. Lal, J. Rahn, A. Nilsson, M. Fisher, M. Kuntz, *Semicond. Sci. Technol.* **2012**, *27*, 094003.
[22] R. Nagarajan, M. Kato, J. Pleumeekers, P. Evans, S. Corzine, S. Hurtt, A. Dentai, S. Murthy, M. Missey, R. Muthiah, R. A. Salvatore, C. Joyner, R. Schneider, M. Ziari, F. Kish, D. Welch, *IEEE J. Sel. Top. Quantum Electron.* **2010**, *16*, 1113.
[23] M. J. Burek, Y. Chu, M. S. Z. Liddy, P. Patel, J. Rochman, S. Meesala, W. Hong, Q. Quan, M. D. Lukin, M. Lončar, *Nat. Commun.* **2014**, *5*, 5718.
[24] P. Latawiec, V. Venkataraman, A. Shams-Ansari, M. Markham, M. Lončar, *Opt. Lett.* **2018**, *43*, 318.
[25] B. Sotillo, V. Bharadwaj, Shivakumar, J. Hadden, S. Rampini, A. Chiappini, T. T. Fernandez, C. Armellini, A. Serpengüzel, M. Ferrari, P. Barclay, R. Ramponi, S. Eaton, *Micromachines* **2017**, *8*, 60.
[26] L. Li, T. Schröder, E. H. Chen, H. Bakhru, D. Englund, *Photonics Nanostructures: Fundam. Appl.* **2015**, *15*, 130.
[27] P. Rath, S. Ummethala, C. Nebel, W. H. P. Pernice, *Phys. Status Solidi* **2015**, *212*, 2385.
[28] J. T. Choy, J. D. B. Bradley, P. B. Deotare, I. B. Burgess, C. C. Evans, E. Mazur, M. Lončar, *Opt. Lett.* **2012**, *37*, 539.
[29] C. Xiong, W. H. P. Pernice, X. Sun, C. Schuck, K. Y. Fong, H. X. Tang, *New J. Phys.* **2012**, *14*, 095014.
[30] B. Desiatov, A. Shams-Ansari, M. Zhang, C. Wang, M. Lončar, *Optica* **2019**, *6*, 380.
[31] R. S. Weis, T. K. Gaylord, *Appl. Phys. A* **1985**, *37*, 191.
[32] A. Boes, B. Corcoran, L. Chang, J. Bowers, A. Mitchell, *Laser Photonics Rev.* **2018**, *12*, 1700256.
[33] P. Rabiei, J. Ma, S. Khan, J. Chiles, S. Fathpour, *Opt. Express* **2013**, *21*, 25573.
[34] A. J. Mercante, P. Yao, S. Shi, G. Schneider, J. Murakowski, D. W. Prather, *Opt. Express* **2016**, *24*, 15590.
[35] C. Wang, M. Zhang, B. Stern, M. Lipson, M. Lončar, *Opt. Express* **2018**, *26*, 1547.
[36] C. Wang, M. Zhang, X. Chen, M. Bertrand, A. Shams-Ansari, S. Chandrasekhar, P. Winzer, M. Lončar, *Nature* **2018**, *562*, 101.
[37] P. Main, P. J. Mosley, W. Ding, L. Zhang, A. V. Gorbach, *Phys. Rev. A* **2016**, *94*, 063844.
[38] N. Montaut, L. Sansoni, E. Meyer-Scott, R. Ricken, V. Quiring, H. Herrmann, C. Silberhorn, *Phys. Rev. Appl.* **2017**, *8*, 024021.
[39] T. Xiang, Y. Li, Y. Zheng, X. Chen, *Opt. Express* **2017**, *25*, 12493.
[40] J. Lu, J. B. Surya, X. Liu, Y. Xu, H. X. Tang, *Opt. Lett.* **2019**, *44*, 1492.
[41] C.-L. Zou, J.-M. Cui, F.-W. Sun, X. Xiong, X.-B. Zou, Z.-F. Han, G.-C. Guo, *Laser Photonics Rev.* **2015**, *9*, 114.
[42] Z. Yu, X. Xi, J. Ma, H. K. Tsang, C.-L. Zou, X. Sun, *Optica* **2019**, *6*, 1342.
[43] Z. Yu, Y. Tong, H. K. Tsang, X. Sun, *Nat. Commun.* **2020**, *11*, 2602.
[44] Z. Yu, X. Sun, *Light: Sci. Appl.* **2020**, *9*, 1.
[45] Z. Yu, Y. Wang, B. Sun, Y. Tong, J.-B. Xu, H. K. Tsang, X. Sun, *Adv. Opt. Mater.* **2019**, *7*, 1901306.
[46] L. Chang, Y. Li, N. Volet, L. Wang, J. Peters, J. E. Bowers, *Optica* **2016**, *3*, 531.
[47] R. Luo, Y. He, H. Liang, M. Li, Q. Lin, *Optica* **2018**, *5*, 1006.
[48] V. G. Dmitriev, G. G. Gurzadyan, D. N. Nikogosyan, *Handbook of Nonlinear Optical Crystals*, Springer, Berlin **2013**.